Process-level Assessment of the Iris Effect over Tropical Oceans

Masato Ito[1] and Hirohiko Masunaga[1]

[1]Nagoya University

November 24, 2022

Abstract

The iris hypothesis suggests a cloud feedback mechanism that a reduction in the tropical anvil cloud fraction (CF) in a warmer climate may act to mitigate the warming by enhanced outgoing longwave radiation. Two different physical processes, one involving precipitation efficiency and the other focusing on upper-tropospheric stability, have been argued in the literature to be responsible for the iris effect. In this study, A-Train observations and reanalysis data are analyzed to assess these two processes. Major findings are as follows: (1) the anvil CF changes evidently with upper-tropospheric stability as expected from the stability iris theory, (2) precipitation efficiency is unlikely to have control on the anvil CF but is related to mid- and low-level CFs, and (3) the day and nighttime cloud radiative effects are expected to largely cancel out when integrated over a diurnal cycle, suggesting a neutral cloud feedback.

Process-level Assessment of the Iris Effect over Tropical Oceans

Masato Ito[1] **and Hirohiko Masunaga**[2]

[1]Graduate School of Environmental Studies, Nagoya University
[2]Institute for Space-Earth Environment Research, Nagoya University

Key Points:

- A-Train satellite observations are analyzed to investigate the physical processes considered to account for the iris effect.
- The anvil cloud fraction reduces with increasing upper-tropospheric stability while unlikely related to precipitation efficiency.
- The cloud radiative effects associated with the stability iris effect are nearly neutral when integrated over a diurnal cycle.

Corresponding author: Hirohiko Masunaga, `masunaga@nagoya-u.jp`

Abstract

The iris hypothesis suggests a cloud feedback mechanism that a reduction in the tropical anvil cloud fraction (CF) in a warmer climate may act to mitigate the warming by enhanced outgoing longwave radiation. Two different physical processes, one involving precipitation efficiency and the other focusing on upper-tropospheric stability, have been argued in the literature to be responsible for the iris effect. In this study, A-Train observations and reanalysis data are analyzed to assess these two processes. Major findings are as follows: (1) the anvil CF changes evidently with upper-tropospheric stability as expected from the stability iris theory, (2) precipitation efficiency is unlikely to have control on the anvil CF but is related to mid- and low-level CFs, and (3) the day and nighttime cloud radiative effects are expected to largely cancel out when integrated over a diurnal cycle, suggesting a neutral cloud feedback.

Plain Language Summary

Tropical anvil clouds, or extensive high clouds produced by deep convection, are known to be a key player in modulating the earth's radiation budget. The iris hypothesis claims that anvil clouds have a stabilizing effect on the climate as they shrink and allow more heat to radiate out to space as the climate warms. The iris hypothesis, however, remains controversial partly because the processes behind it have not been well validated against observations. We analyze satellite observations and reanalysis data to test two known theories on the processes explaining the iris effect. The results show that a theory focusing on the air temperature structure around anvil clouds is likely at work in the tropical atmosphere, although the anvil's warming and cooling effects would offset each other during the whole day and night.

1 Introduction

Cirrus clouds prevail over tropical oceans, modulating the earth's energy budget through the reflection of solar radiation and the absorption and emission of longwave radiation. Of particular interest are anvil cirrus clouds produced by detrainment from deep convection, which are a key player in the potential interactions between tropical convective dynamics and cloud radiative effects (CREs). There is rich literature on the cloud feedback involving the interactions of convection, clouds, and radiation. Ramanathan and Collins (1991) argued that the shielding of solar radiation by anvil clouds overwhelm the enhanced greenhouse effect in a moist, convectively active atmosphere over warm ocean, acting as a natural thermostat regulating sea surface temperature (SST). Other hypotheses put focus on the longwave effect of anvil clouds. Lindzen et al. (2001) proposed an "iris" mechanism that anvil clouds shrink and allow more warm radiation to escape out to space as SST increases, resulting in a negative feedback on SST. The thermostat and iris hypotheses, although very different in mechanism and each challenged by a series of criticisms (e.g. Pierrehumbert, 1995; Hartmann & Michelsen, 2002), share a common ground in that anvil clouds play a role in stabilizing the climate system.

Another line of research (Hartmann & Larson, 2002; Zelinka & Hartmann, 2010) explored the possibility that the longwave effect of anvil clouds could give rise to a positive feedback rather than a stabilizing one. In the hypotheses known as fixed anvil temperature (FAT) and proportionately higher anvil temperature (PHAT), anvil cloud temperature remains nearly constant regardless of a surface warming, so that outgoing longwave radiation (OLR) cannot efficiently remove an extra heat associated with the warming. The FAT/PHAT theory is built upon an upper-tropospheric thermodynamic and mass balance consideration, interrelating a chain of processes such as temperature-limited moisture, radiative cooling, static stability, and horizontal divergence/convergence. Elements of this idea were reorganized into a "stability iris" theory (Bony et al., 2016) in light of a growing interest in convective self-aggregation (see reviews by Wing et al., 2017;

Holloway et al., 2017). The stability iris hypothesis predicts that anvil cloud cover should be reduced as the result of an enhanced upper-tropospheric stability in a warmer climate. The stability iris resembles the iris hypothesis as originally devised by Lindzen et al. (2001), whereas the underlying mechanism is entirely renewed.

Mauritsen and Stevens (2015) shed new light on the iris effect in the context of climate and hydrological sensitivities, demonstrating that climate model simulations are improved if the conversion from cloud water to precipitation is tuned so as to accelerate with a surface warming. Such a temperature dependence of precipitation efficiency was speculated by Lindzen et al. (2001) as a possible driver of the iris effect, although not supported to date by firm evidence (Sui et al., 2020). Rapp et al. (2005), Lin et al. (2006), and Choi et al. (2017) each evaluated precipitation efficiency in different manners and reached mixed conclusions regarding the iris effect. Observational evidence supportive of the stability iris was presented by Saint-Lu et al. (2020), although the consequences on CREs have yet to be examined.

A primary motivation of the present paper is to investigate the physical processes underlying the iris effect, if the iris exists in the real atmosphere. We do not seek observational evidence for the feedback hypothesis itself, given the difficulty of assessing the long-term regulation of SST with short-term observations. Our focus is restricted to the process-level linkage of precipitation efficiency or stability with the anvil cloud cover and CREs.

At the heart of the analysis lie CloudSat radar and Cloud-Aerosol Lidar and Infrared Pathfinder Satellite Observation (CALIPSO) lidar measurements to sample anvil clouds and the parent convective clouds at the same time. This approach enables to preclude in-situ cirrus without direct relevance to convective dynamics, which amount to more than a half of the whole tropical cirrus (Luo & Rossow, 2004). A-Train satellite measurements and the European Centre for Medium-Range Weather Forecasts Reanalysis version 5 (ERA5) data are combined to evaluate the ratio of cloud water to precipitation (R_{CP}), introduced as a proxy of precipitation efficiency, and upper-tropospheric stability (S_{UT}). A composite analysis is then carried out to explore the dependence of anvil cloud properties on R_{CP} and S_{UT}. The net radiative effect is analyzed as well as the longwave effect for examining to what extent the shortwave component counteracts the longwave iris effect.

2 Data and Method

The Aqua satellite carries six instruments including Advanced Microwave Scanning Radiometer for the Earth Observing System (AMSR-E), Clouds and the Earth's Radiant Energy System (CERES), and Moderate Resolution Imaging Spectroradiometer (MODIS). The Aqua, CloudSat, and CALIPSO satellites, as part of the A-Train constellation, make near-simultaneous observations. The CALIPSO, CloudSat, CERES, and MODIS (CCCM) Release D1 product integrates observations from these instruments to yield the vertical structure of clouds and the in-cloud and clear-sky radiative flux estimates (Kato et al., 2011). The CCCM algorithm defines cloud fraction (CF) as the fractional coverage of CloudSat- and CALIPSO-detected clouds within each nadir ∼20-km CERES footprint. The in-cloud radiative flux is computed with the cloud optical properties diagnosed from the CloudSat, CALIPSO, and MODIS products combined together. The AMSR-E daily (practically instantaneous) product by Remote Sensing Systems (RSS) provide precipitation and liquid water path (LWP) estimates (Wentz, 2013; Hilburn & Wentz, 2008). Upper-tropospheric stability is quantified using the ERA5 data (Hersbach et al., 2020).

The CCCM cloud and radiative properties are accumulated on a quarter-degree grid to match the AMSR-E and ERA5 datasets. Only the portions of AMSR-E and ERA5 data intersected by CloudSat/CALIPSO ground tracks are sampled for the analysis. Deep

convection is defined to occur when CF exceeds 0.5 at all levels between 1 and 16.6 km in altitude for a given CCCM column. The lower limit of 1 km is chosen to be above the lifting condensation level (a proxy of convective cloud base) over tropical oceans (typically about 500 m), and the upper boundary of 16.6 km is an altitude close to the tropical tropopause. In case that a sequence of CCCM pixels in row are identified as deep convection, the consecutive pixels are combined into a single convective event with their midpoint defined to be the geographical center of deep convection. Lower or higher CF thresholds than 0.5 do not qualitatively alter main conclusions. The cloud properties and atmospheric profiles within $\pm 5°$ along CloudSat/CALIPSO tracks around each convection center are recorded for the composite analysis described next.

Composite analysis is carried out to look into the statistical characteristics of deep convection and the associated cloud properties and atmospheric states. Satellite measurements sampled around the deep convection centers are averaged together into a two-dimensional composite space comprised of along-track distance from the convection center and altitude. The compositing method is similar to the technique devised by Igel et al. (2014) but is substantially simplified. The primary interest of Igel et al. (2014) lay in the anvil cloud structure and how it changes with SST beneath, while the present work is focused more on the resulting radiative effects in reference to R_{CP} and S_{UT} (precise definitions are given later). To this end, composite samples are broken down by quartiles of R_{CP} and of S_{UT}, with outliers (i.e., below the first quartile minus 1.5×IQR or above the third quartile plus 1.5×IQR, where IQR is the interquartile range) removed from the samples.

Precipitation efficiency is conventionally defined by the ratio of precipitation to either the large-scale moisture influx or the condensation rate (Sui et al., 2007). The variables appearing in the denominator, however, are difficult to evaluate from satellite observations alone. As a workaround, precipitation efficiency can be substituted by a combination of cloud water mass (or cloud size) and precipitation, both of which are available from satellite measurements (e.g., Lau & Wu, 2003; Rapp et al., 2005). In the present work, the ratio of precipitation P to column-integrated cloud water,

$$R_{\mathrm{CP}} \equiv \frac{P}{\mathrm{LWP} + \mathrm{IWP}} \, , \tag{1}$$

is employed as a proxy of precipitation efficiency in the current analysis. Here liquid water path (LWP) is obtained from the AMSR-E product, while ice water path (IWP) is estimated as the vertical integral of CCCM cloud ice water content. This compromise is necessitated by the technical limitations in satellite measurement capabilities that (1) microwave radiometry is insensitive to ice clouds and (2) CloudSat radar and CALIPSO lidar echoes are often heavily attenuated before reaching down to the liquid layer inside deep convective clouds. For every deep convection sample, P, LWP, and IWP are each averaged within $\pm 2°$ about the convection center before combining into R_{CP} by (1).

Upper-tropospheric stability is quantified as,

$$S_{\mathrm{UT}} = \frac{RT}{c_p p} - \frac{\partial T}{\partial p} \quad \text{at 200 hPa} \, , \tag{2}$$

where R and c_p are the gas constant and specific heat of dry air, respectively, T is air temperature, and p is pressure. Throughout this study, S_{UT} is defined only where AMSR-E precipitation is zero and ERA5 pressure velocity (ω) is positive so that S_{UT} is related to the radiatively driven subsidence as formulated in the stability iris hypothesis.

The study period spans four years from 1 January 2007 to 31 December 2010. The target region is global tropical oceans over all longitudes but bound in latitude between 20°S and 20°N. This choice of latitudes is intended to ensure that the analysis is limited to the tropics by factoring out unwanted influences of the pronounced regional gradient from tropics to subtropics. Additional analyses with latitudinal boundaries raised

to 30° did not essentially alter the results in any case because the present compositing method is conditioned on the occurrence of deep convection. The total sample size is 3677 for the R_{CP} composite and 3549 for the S_{UT} composite, of which roughly two thirds are from descending (1:30) tracks and the other one third from ascending (13:30) overpasses.

3 Results

3.1 Composite Cloud Fraction

The composite vertical structure of CF for different stability environments is plotted in Fig. 1. The four panels in the top row represent very unstable ($S_{\mathrm{UT}} < S_1$), moderately unstable ($S_1 < S_{\mathrm{UT}} < S_2$), moderately stable ($S_2 < S_{\mathrm{UT}} < S_3$), and very stable ($S_3 < S_{\mathrm{UT}}$) upper troposphere, where $S_1 = 27.4$ mK hPa^{-1}, $S_2 = 34.3$ mK hPa^{-1}, and $S_3 = 42.0$ mK hPa^{-1} are the first, second, and third quartiles of S_{UT}, respectively. All the four cases share a common feature that anvil clouds are spread extensively above 200 hPa from the deep convection towering at the center, except that the anvil cloud extent narrows systematically with increasing S_{UT}. The dependence on S_{UT} is clearly evidenced by Fig. 1e, where the anvil CF at the level of maximum convergence is shown. Here convergence profiles were sampled from rain-free subsidence areas (i.e., conditioned on $P = 0$ and $\omega > 0$ as was for S_{UT}) and then averaged together at each level in composite space. The composite convergence profiles (Fig. 1f) have a maximum near the tropopause with its magnitude diminishing with increasing S_{UT}. The interrelationship among the anvil CF, S_{UT}, and upper-tropospheric convergence derived from Fig. 1 is in line with the expectations of the stability iris theory (Bony et al., 2016).

The dependence of CF on R_{CP} is shown in Fig. 2. The three quartiles of R_{CP} are $R_1 = 0.619$ h^{-1}, $R_2 = 0.942$ h^{-1}, and $R_3 = 1.30$ h^{-1}. CF exhibits a slight but consistent enhancement with increasing R_{CP} at levels lower than $\sim$400 hPa. In contrast, upper-tropospheric CF hardly varies across the whole range of R_{CP}. It follows that an enhancement in precipitation efficiency is unlikely to have appreciable consequences on the hor-
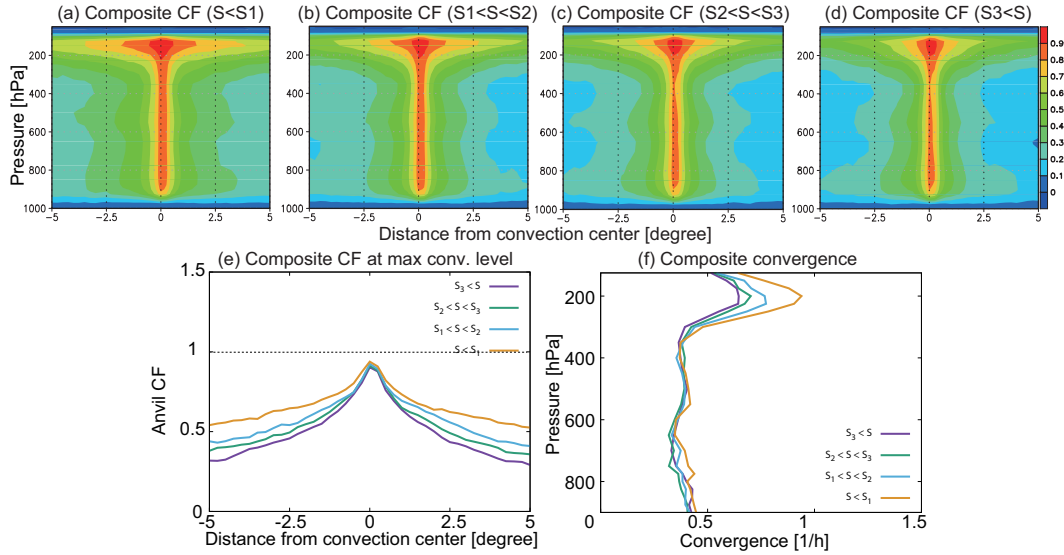
Figure 1. (a) Composite cloud fraction (CF) for $S_{\mathrm{UT}} < S_1$, (b) CF for $S_1 < S_{\mathrm{UT}} < S_2$, (c) CF for $S_2 < S_{\mathrm{UT}} < S_3$, and (d) CF for $S_3 < S_{\mathrm{UT}}$, where S_1–S_3 are the first to third quartiles of S_{UT}. (e) CF at the level of maximum convergence for different stabilities. (f) Convergence averaged horizontally at each level over rain-free subsidence areas within $\pm 5°$ about the convection center.
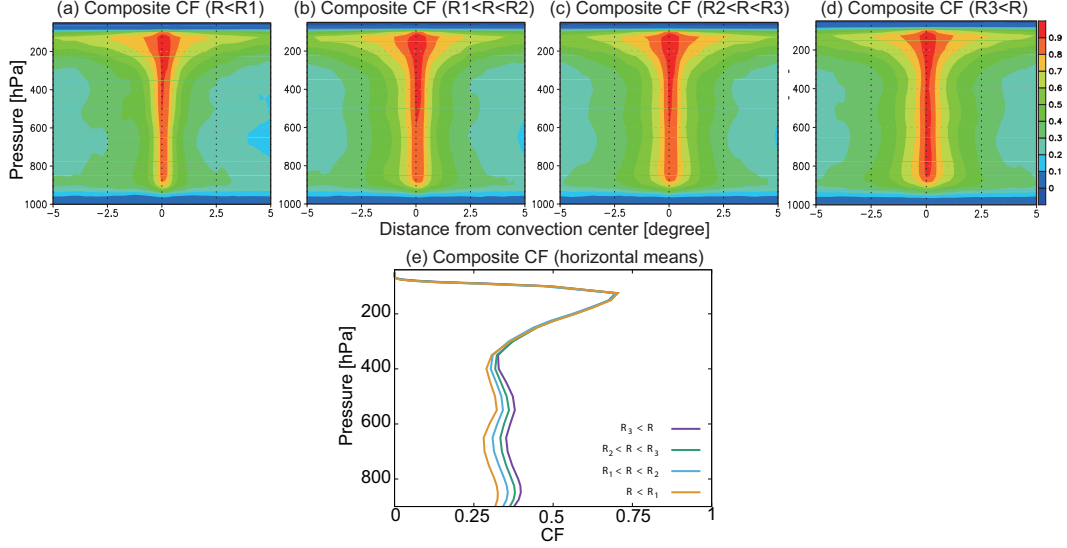
Figure 2. (a) Composite cloud fraction (CF) for $R_{CP} < R_1$, (b) CF for $R_1 < R_{CP} < R_2$, (c) CF for $R_2 < R_{CP} < R_3$, and (d) CF for $R_3 < R_{CP}$, where R_1–R_3 are the first to third quartiles of R_{CP}. (e) CF for different stabilities, averaged horizontally at each level over $\pm 5°$ about the convection center.

izontal extent of anvil clouds, although leading to a modest increase of CF in the mid and lower tropospheres.

3.2 Cloud Radiative Effects

Next examined are the impacts of S_{UP} and R_{CP} on the CREs associated with tropical deep convection. The net CRE at the top of the atmosphere (TOA) is,

$$\text{CRE} = F_{SW}^{clr} - F_{SW}^{all} + F_{LW}^{clr} - F_{LW}^{all} , \tag{3}$$

where F is upwelling radiative flux at TOA, SW and LW denote shortwave and longwave, "clr" and "all" stand for clear and all skies, respectively. Every term on the rhs is available from the CCCM product, in which the clear-sky component is a synthetic estimate computed with all clouds taken out. CRE is sorted by S_{UT} and R_{CP} as done for the composite analysis in the previous section, except that this time the convection-anvil samples are broken down into finer bins of $\Delta S_{UT} = 5$ mK hPa^{-1} and $\Delta R_{CP} = 0.05$ h^{-1} instead of quartiles.

Figures 3a-d show the scatter plots of the statistical relationship between the anvil CF and the net CRE at TOA. The midnight CRE from descending satellite tracks (Fig. 3a), consisting exclusively of longwave cloud warming, is tightly coupled with the anvil CF. An enhancement of CRE is accounted for by an increase of the anvil CF, which accompanies a reduction of upper-tropospheric stability (from warm to cold colors) as we have seen in Fig. 1. Afternoon observations of the net CRE (Fig. 3a), by contrast, imply a striking shortwave effect largely overwhelming the longwave effect. When the morning and afternoon measurements are combined together, the resulting CRE tends to fall on the negative side (i.e., have a potential of cooling the planet) with its magnitude weakly increasing with the anvil CF (Fig. 3c).

This day-night combined CRE, however, is not an adequate measure of the daily mean CRE because the daytime equatorial crossing time of 13:30 is nearly the peak hour
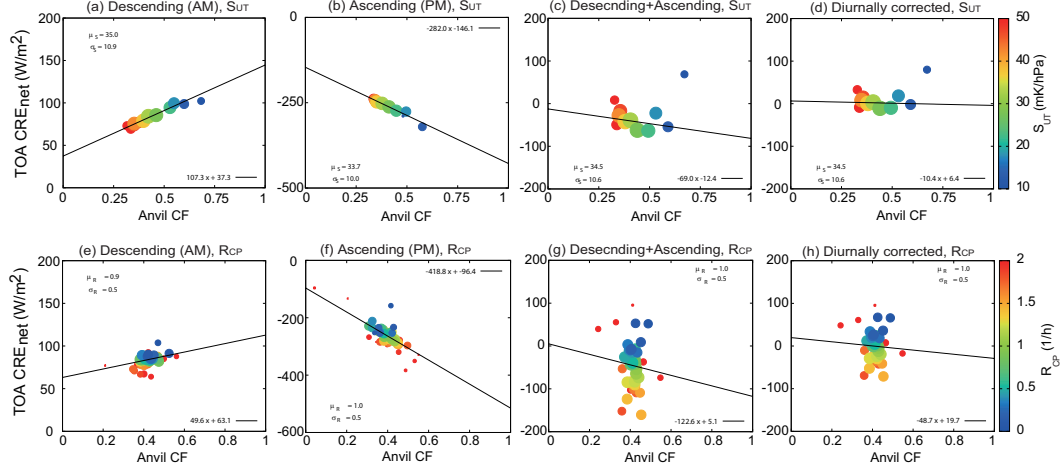
Figure 3. Top row (a-d): scatter plots between the anvil CF and the net CRE at TOA sorted by S_{UT} for (a) descending tracks (midnight), (b) ascending tracks (afternoon), (c) descending and ascending tracks combined, and (d) daily mean (diurnally corrected) estimates (see text for details). Points represent different values of S_{UT} as indicated by color scale on the right. The point size is proportional to the sample size for each bin having a fixed width of $\Delta S_{UT} = 5$ mK hPa^{-1}. The mean μ, standard deviation σ, and linear regression coefficients are shown in each panel. Bottom row (e-h): As the top row but sorted by R_{CP} with a bin width of $\Delta R_{CP} = 0.05$ h^{-1}.

of incoming solar radiation. To remedy this, a simplistic diurnal correction is applied assuming a semi-sinusoidal diurnal cycle of solar irradiation,

$$\overline{F}_{SW} = \frac{\pi I_0}{12} \int_6^{18} \left[-\cos\left(\frac{\pi t}{12}\right) \right] dt = 2I_0 , \tag{4}$$

where $\overline{F}_{SW}$ is the daily mean shortwave flux and t is local time in hour (e.g., Shinoda & Hendon, 1998). The amplitude πI_0 is eliminated with a given A-Train measurement at $t = 13.5$ h or $F_{SW}^{obs} = -\pi I_0 \cos(13.5\pi/12)$ as

$$\overline{F}_{SW} = -\frac{2F_{SW}^{obs}}{\pi \cos(13.5\pi/12)} \approx 0.638 F_{SW}^{obs} . \tag{5}$$

Equation (5) relies on a number of naive assumptions (e.g., cloud properties do not vary with local time) and is only intended to offer an approximate (yet useful) correction factor. Figure 3d shows the daily mean net CRE with the above correction applied. Interestingly, the diurnally corrected shortwave CRE almost precisely offsets the longwave CRE for almost all anvil CFs.

The scatter plots broken down by R_{CP} are presented in Fig. 3e-h. The correlation of the anvil CF with the net CRE is recognizable when midnight and afternoon observations are separated, whereas no longer visually discernible in the daily mean (Fig. 3h). Unlike the S_{UT} cases, color gradient is primarily vertical across the line of zero daily-mean CRE, implying that a low (high) R_{CP} is likely to accompany a positive (negative) net CRE for reasons unrelated to anvil clouds. This correlation is presumably ascribed to variability in the mid- to low-level CFs as was found in Fig. 2e.

4 Conclusion and Discussion

A-Train satellite observations and ERA5 datasets were analyzed to investigate the physical processes considered to be crucial for the iris effect, namely the cloud-water to precipitation ratio R_{CP} (a substitute for precipitation efficiency) and upper-tropospheric stability S_{UT}. Composite analysis was carried out to illustrate the spatial structure of deep convective clouds and the accompanying anvil clouds, and to examine how CREs vary with the anvil CF. The composite samples are separated by S_{UT} and R_{CP} in search of evidence for the possible roles of these parameters behind the iris effect.

A main conclusion is, in line with a previous study (Saint-Lu et al., 2020), that S_{UT} is clearly linked with the anvil CF as hypothesized by the stability iris theory. To the contrary, the anvil CF is invariant over the whole range of R_{CP}, although the mid- to low-level CFs modestly but systematically increase with R_{CP}. A possible explanation for this may be given in light of the mesoscale organization of convective systems. Sui et al. (2020) argued that precipitation efficiency rises as the degree of convective organization increases (that is, the stratiform rain fraction becomes higher). Choi et al. (2017) underscored the key roles of stratiform rain clouds in the context of the iris effect. Changes in the mid- to low-level CFs with R_{CP} are presumably relevant to the observed modulation in CREs, although in a way at odds with what Lindzen et al. (2001) hypothesized with precipitation efficiency.

The current work does not seek evidence for the climatic consequences of the processes investigated here, but nevertheless it would be beneficial to briefly discuss the implications for cloud feedback. The longwave CRE at midnight infers a negative feedback just as predicted by the stability iris hypothesis, while the noontime CRE suggests a weak positive feedback in which the shortwave heating owing to a shrinkage of anvil clouds slightly outruns the longwave effect. These competing effects are estimated to largely cancel each other out when averaged over a diurnal cycle. The stability iris effect is suggested to be nearly radiatively neutral in a climatological context, although away from neutrality on subdaily time scales.

The shortwave and longwave CREs of tropical cirrus have been long known to have a tendency of offsetting each other (e.g., Ramanathan et al., 1989; Hartmann et al., 2001). The near cancellation of CRE is rarely achieved on a cloud-by-cloud basis but results from an ensemble of clouds with different altitudes and optical depths averaged together (Hartmann & Berry, 2017). The dynamical, microphysical, and radiative properties of anvil clouds are intertwined with the convective life cycle (Takahashi et al., 2017; Masunaga & Bony, 2018; Gasparini et al., 2019), and so would be the transient CRE imbalances on a subdaily time scale. These short-term processes remain a missing piece of puzzle to draw the whole picture of the anvil cloud feedback.

Data Availability Statement

Acknowledgments

References

Bony, S., Stevens, B., Coppin, D., Becker, T., Reed, K. A., Voigt, A., & Medeiros, B. (2016). Thermodynamic control of anvil cloud amount. *Proc. Natl. Acad. Sci. USA*, *113*, 8927-8932. doi: 10.1073/pnas.1601472113

Choi, Y.-S., Kim, W., Yeh, S.-W., Masunaga, H., Kwon, M.-J., Jo, H.-S., & Huang, L. (2017). Revisiting the iris effect of tropical cirrus clouds with TRMM and A-Train satellite data. *J. Geophys. Res.*, *122*, 5917-5931. doi: 10.1002/2016JD025827

Gasparini, B., Blossey, P. N., Hartmann, D. L., Lin, G., & Fan, J. (2019). What drives the life cycle of tropical anvil clouds? *J. Adv. Model. Earth Syst.*, *11*, 2586-2605. doi: 10.1029/2019MS001736

Hartmann, D. L., & Berry, S. E. (2017). The balanced radiative effect of tropical anvil clouds. *J. Geophys. Res.*, *122*, 5003-5020. doi: 10.1002/2017JD026460

Hartmann, D. L., & Larson, K. (2002). An important constraint on tropical cloud-climate feedback. *Geophys. Res. Lett.*, *29*. doi: 10.1029/2002GL015835

Hartmann, D. L., & Michelsen, M. L. (2002). No evidence for iris. *Bull. Amer. Meteor. Soc.*, *83*, 249-254.

Hartmann, D. L., Moy, L. A., & Fu, Q. (2001). Tropical convection and the energy balance at the top of the atmosphere. *J. Climate*, *14*, 4495-4511.

Hersbach, H., Bell, B., Berrisford, P., Biavati, G., Horányi, A., Muñoz Sabater, J., ... Thépaut, J.-N. (2018). *ERA5 hourly data on pressure levels from 1979 to present.* Copernicus Climate Change Service (C3S) Climate Data Store (CDS). doi: 10.24381/cds.bd0915c6

Hersbach, H., Bell, B., Berrisford, P., Hirahara, S., Horányi, A., Muñoz Sabater, J., ... Thépaut, J.-N. (2020). The ERA5 global reanalysis. *Quart. J. Roy. Meteor. Soc.*, *146*, 1999-2049. doi: 10.1002/qj.3803

Hilburn, K. A., & Wentz, F. J. (2008). Intercalibrated passive microwave rain products from the unified microwave ocean retrieval algorithm (UMORA). *J. Appl. Meteor. Climatol.*, *47*, 778-794. doi: 10.1175/2007JAMC1635.1

Holloway, C. E., Wing, A. A., Bony, S., Muller, C., Masunaga, H., L'Ecuyer, T. S., ... Zuidema, P. (2017). Observing convective aggregation. *Surv. Geophys.*, *38*, 1199-1236. doi: 10.1007/s10712-017-9419-1

Igel, M. R., Drager, A. J., & van den Heever, S. C. (2014). A CloudSat cloud object partitioning technique and assessment and integration of deep convective anvil sensitivities to sea surface temperature. *J. Geophys. Res.*, *119*, 10515-10535. doi: 10.1002/2014JD021717

Kato, S., Rose, F. G., Sun-Mack, S., Miller, W. F., Chen, Y., Rutan, D. A., ... Collins, W. D. (2011). Improvements of top-of-atmosphere and surface irradiance computations with CALIPSO-, CloudSat-, and MODIS-derived cloud and aerosol properties. *J. Geophys. Res.*, *116*(D19). doi: 10.1029/2011JD016050

Lau, K. M., & Wu, H. T. (2003). Warm rain processes over tropical oceans and climate implications. *Geophys. Res. Lett.*, *30*, 2290. doi: 10.1029/2003GL018567

Lin, B., Wielicki, B. A., Minnis, P., Chambers, L., Xu, K.-M., Hu, Y., & Fan, A. (2006). The effect of environmental conditions on tropical deep convective systems observed from the TRMM satellite. *J. Climate*, *19*, 5745-5761. doi: 10.1175/JCLI3940.1

Lindzen, R. S., Chou, M.-D., & Hou, A. Y. (2001). Does the Earth have an adaptive infrared iris? *Bull. Amer. Meteor. Soc.*, *82*, 417-432.

Luo, Z., & Rossow, W. B. (2004). Characterizing tropical cirrus life cycle, evolution, and interaction with upper-tropospheric water vapor using Lagrangian trajectory analysis of satellite observations. *J. Climate*, *17*, 4541-4563.

Masunaga, H., & Bony, S. (2018). Radiative invigoration of tropical convection by preceding cirrus clouds. *J. Atmos. Sci.*, *75*, 1327-1342. doi: 10.1002/2016MS000855

Mauritsen, T., & Stevens, B. (2015). Missing iris effect as a possible cause of muted hydrological change and high climate sensitivity in models. *Nature Geosci.*, *8*, 346-351. doi: 10.1038/ngeo2414

NASA/LARC/SD/ASDC. (2011). *CERES A-Train Integrated CALIPSO, Cloud-Sat, CERES, and MODIS (CCCM) Merged Release D1.* NASA Langley Atmospheric Science Data Center DAAC. Retrieved from https://doi.org/10.5067/AQUA/CERES/CCCM-FM3-MODIS-CAL-CS_L2.RELD1

Pierrehumbert, R. T. (1995). Thermostats, radiator fins, and the local runaway greenhouse. *J. Atmos. Sci.*, *52*, 1784-1806.

Ramanathan, V., Cess, R. D., Harrison, E. F., Minnis, P., Barkstrom, B. R., Ahmad, E., & Hartmann, D. (1989). Cloud-radiative forcing and climate: Results from the Earth Radiation Budget Experiment. *Science*, *243*, 57-63. doi: 10.1126/science.243.4887.57

Ramanathan, V., & Collins, W. (1991). Thermodynamic regulation of ocean warming by cirrus clouds deduced from observations of the 1987 El Niño. *Nature*, *351*, 27-32.

Rapp, A. D., Kummerow, C., Berg, W., & Griffith, B. (2005). An evaluation of the proposed mechanism of the adaptive infrared iris hypothesis using TRMM VIRS and PR measurements. *J. Climate*, *18*, 4185-4194. doi: 10.1175/JCLI3528.1

Saint-Lu, M., Bony, S., & Dufresne, J.-L. (2020). Observational evidence for a stability iris effect in the tropics. *Geophys. Res. Lett.*, *47*, e2020GL089059. doi: 10.1029/2020GL089059

Shinoda, T., & Hendon, H. H. (1998). Mixed layer modeling of intraseasonal variability in the tropical western Pacific and Indian oceans. *J. Climate*, *11*, 2668-2685.

Sui, C.-H., Li, X., & Yang, M.-J. (2007). On the definition of precipitation efficiency. *J. Atmos. Sci.*, *64*, 4506-4513.

Sui, C.-H., Satoh, M., & Suzuki, K. (2020). Precipitation efficiency and its role in cloud-radiative feedbacks to climate variability. *J. Meteor. Soc. Japan*, *98*, 261-282. doi: 10.2151/jmsj.2020-024

Takahashi, H., Luo, Z. J., & Stephens, G. L. (2017). Level of neutral buoyancy, deep convective outflow, and convective core: New perspectives based on 5 years of CloudSat data. *J. Geophys. Res.*, *122*, 2958-2969. doi: 10.1002/2016JD025969

Wentz, F. (2013). *SSM/I version-7 calibration report* (Tech. Rep. No. 011012). Sant Rosa, CA, USA: Remote Sensing Systems.

Wing, A. A., Emanuel, K., Holloway, C. E., & Muller, C. (2017). Convective self-aggregation in numerical simulations: A review. *Surv. Geophys.*, *38*, 1-25. doi: 10.1007/s10712-017-9408-4

Zelinka, M. D., & Hartmann, D. L. (2010). Why is longwave cloud feedback positive? *J. Geophys. Res.*, *115*(D16). doi: 10.1029/2010JD013817
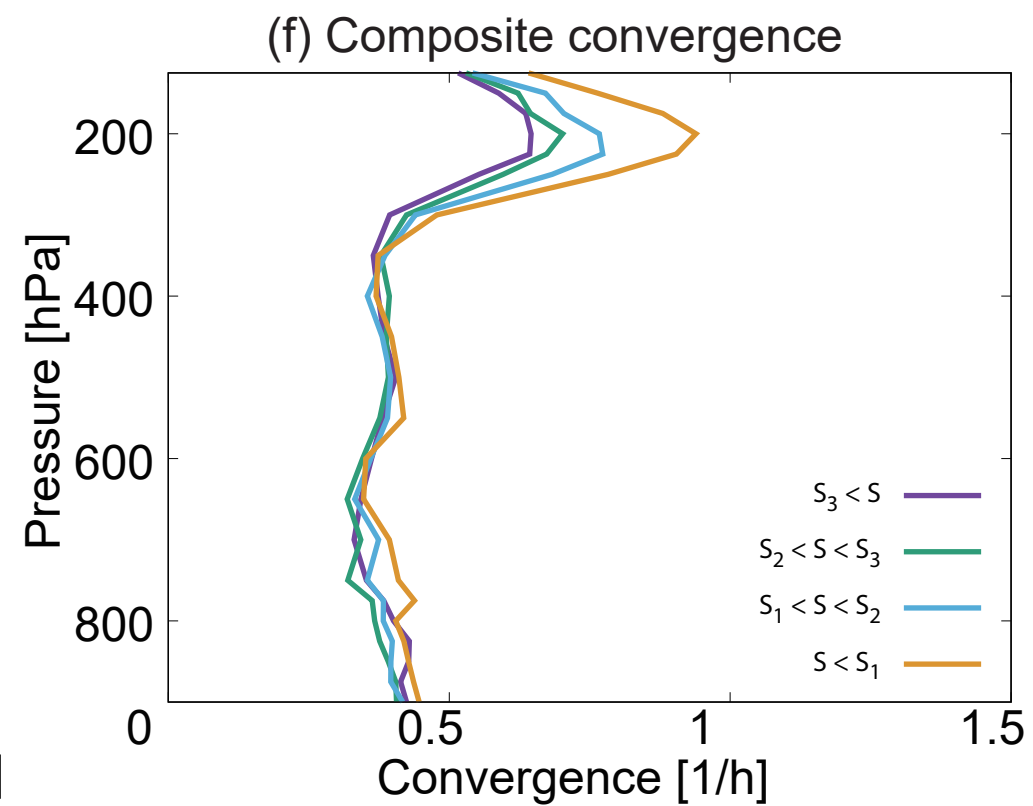
Figure 1.

(a) Composite CF (S<S1) (b) Composite CF (S1<S<S2) (c) Composite CF (S2<S<S3) (d) Composite CF (S3<S)

(e) Composite CF at max conv. level

(f) Composite convergence

Figure 2.

(a) Composite CF (R<R1) (b) Composite CF (R1<R<R2) (c) Composite CF (R2<R<R3) (d) Composite CF (R3<R)

Distance from convection center [degree]

(e) Composite CF (horizontal means)

$R_3 < R$
$R_2 < R < R_3$
$R_1 < R < R_2$
$R < R_1$

Figure 3.

(a) Descending (AM), S_{UT}
$\mu_S = 35.0$
$\sigma_S = 10.9$
$107.3\,x + 37.3$

(b) Ascending (PM), S_{UT}
$-282.0\,x - 146.1$
$\mu_S = 33.7$
$\sigma_S = 10.0$

(c) Desecnding+Ascending, S_{UT}
$\mu_S = 34.5$
$\sigma_S = 10.6$
$-69.0\,x - 12.4$

(d) Diurnally corrected, S_{UT}
$\mu_S = 34.5$
$\sigma_S = 10.6$
$-10.4\,x + 6.4$

S_{UT} (mK/hPa)

(e) Descending (AM), R_{CP}
$\mu_R = 0.9$
$\sigma_R = 0.5$
$49.6\,x + 63.1$

(f) Ascending (PM), R_{CP}
$-418.8\,x + -96.4$
$\mu_R = 1.0$
$\sigma_R = 0.5$

(g) Desecnding+Ascending, R_{CP}
$\mu_R = 1.0$
$\sigma_R = 0.5$
$-122.6\,x + 5.1$

(h) Diurnally corrected, R_{CP}
$\mu_R = 1.0$
$\sigma_R = 0.5$
$-48.7\,x + 19.7$

R_{CP} (1/h)

TOA CRE_{net} (W/m^2)

Anvil CF